

A TRANSITING BROWN DWARF IN A 2 HOUR ORBIT

KAREEM EL-BADRY ¹, KEVIN B. BURDGE ², JAN VAN ROESTEL ³, AND ANTONIO C. RODRIGUEZ ¹

¹Department of Astronomy, California Institute of Technology, 1200 E. California Blvd., Pasadena, CA 91125, USA

²MIT Kavli Institute for Astrophysics and Space Research, 77 Massachusetts Ave., Cambridge, MA 02139, USA and

³Anton Pannekoek Institute for Astronomy, University of Amsterdam, 1090 GE Amsterdam, The Netherlands

Version September 15, 2023

ABSTRACT

We report the discovery of ZTF J2020+5033, a high-mass brown dwarf (BD) transiting a low-mass star with an orbital period of 1.90 hours. Phase-resolved spectroscopy, optical and infrared light curves, and precise astrometry from *Gaia* allow us to constrain the masses, radii, and temperatures of both components with few-percent precision. We infer a BD mass of $M_{\text{BD}} = 80.1 \pm 1.6 M_{\text{J}}$, almost exactly at the stellar/substellar boundary, and a moderately inflated radius, $R_{\text{BD}} = 1.05 \pm 0.02 R_{\text{J}}$. The transiting object’s temperature, $T_{\text{eff}} \approx 1700$ K, is well-constrained by the depth of the infrared secondary eclipse and strongly suggests it is a BD. The system’s high tangential velocity ($v_{\perp} = 98 \text{ km s}^{-1}$) and thick disk-like Galactic orbit imply the binary is old; its close distance ($d \approx 140$ pc) suggests that BDs in short-period orbits are relatively common. ZTF J2020+5033 is the shortest-period known transiting BD by more than a factor of 7. Today, the entire binary would comfortably fit inside the Sun. However, both components must have been considerably larger in youth, implying that the orbit has shrunk by at least a factor of ~ 5 since formation. The simplest explanation is that magnetic braking continues to operate efficiently in at least some low-mass stars and BDs.

Subject headings: brown dwarfs – binaries: close – binaries: eclipsing

1. INTRODUCTION

Brown dwarfs (BDs) are degenerate substellar objects with masses ranging roughly from 13 to 80 M_{J} , between giant planets and stars, and radii similar to Jupiter. The temperatures in BD cores are not high enough to sustain long-term hydrogen fusion, so BDs cool as they age, slowly radiating away energy, contracting, and fading.

A large majority of the ~ 5000 known BDs are isolated and were discovered via their thermal emission in infrared surveys (e.g. Gelino et al. 2009; Mace 2014; Kirkpatrick et al. 2021; Aganze et al. 2022). BDs in binaries are surprisingly rare: only about 1% of solar-type and lower-mass stars have BD companions within a few au, making BD companions significantly less common than either higher-mass stellar companions or lower-mass planets (Marcy & Butler 2000; Grether & Lineweaver 2006; Raghavan et al. 2010; Triaud et al. 2017). Several theoretical explanations for this “brown dwarf desert” have been proposed, with most invoking different formation mechanisms for close-in giant planets, BDs, and low-mass stars (e.g. Stamatellos & Whitworth 2009; Ma & Ge 2014).

BDs in binaries are sought after both as probes of the star formation process and as laboratories in which to measure BD masses and radii. About 50 transiting BDs have been discovered in the last decade (see Carmichael 2023, for a recent summary). Most of these systems were initially discovered as transiting planet candidates by surveys including WASP (Pollacco et al. 2006), *CoRoT* (Baglin et al. 2006), *Kepler* (Borucki et al. 2010), and *TESS* (Ricker et al. 2015), and were identified as BDs after radial velocity (RV) follow-up. Radius measurements of transiting BDs have revealed significant scatter in the

distribution of observed radii at fixed mass, even among BDs with similar ages and compositions (e.g. Bouchy et al. 2010; Hodžić et al. 2018; Carmichael et al. 2020; Casewell et al. 2020c,a; Acton et al. 2021). On average, observed transiting BDs are 5-10% larger than predicted by models. The degree of this “radius inflation” is only weakly correlated with irradiation from the BDs’ stellar companions (Casewell et al. 2020c; Sainsbury-Martinez et al. 2021). It is reminiscent of the radius inflation observed in many M dwarfs (López-Morales & Ribas 2005; Bayless & Orosz 2006; Irwin et al. 2009; Cruz et al. 2018; Kesseli et al. 2018; Parsons et al. 2018; Jaehmig et al. 2019; Jackson et al. 2019), which has been attributed to a variety of processes including magnetic inhibition of convection, flux-blocking by starspots, and tidal heating.

Most of the known transiting BDs have orbital periods between 1 and 10 days and transit solar-type main sequence stars. The shortest-period BD + main sequence binary discovered so far has an orbital period of 0.56 days (Parviainen et al. 2020). It is uncertain whether BDs are expected to exist in significantly shorter orbits. On the one hand, BDs can have high densities and can – if paired with another BD or low-mass star – fit into orbits with periods as short as ≈ 40 minutes (e.g. Rappaport et al. 2021). On the other, evolutionary models struggle to explain the formation of short-period BD and M dwarf binaries: most models assume that magnetic braking – which is thought to be the dominant mechanism through which low-mass binaries can lose angular momentum after their formation – is inefficient below the fully-convective boundary (e.g. Rappaport et al. 1983; Stepien 2006; Reiners & Basri 2008; Schreiber et al. 2010; Garraffo et al. 2015), and thus that low-mass binary orbits should not shrink significantly after formation. Since BDs and low-mass stars have $\gtrsim 1 R_{\odot}$ radii at young ages

($\lesssim 1$ Myr, e.g. Chabrier & Baraffe 1997; Phillips et al. 2020), they cannot reach $P_{\text{orb}} \lesssim 1$ day without some angular momentum loss mechanism.

Magnetic braking is a process through which stellar winds carry away angular momentum when magnetic fields cause them to co-rotate with the stellar surface (e.g. Schatzman 1962). In close binaries, tides keep the component stars rotating on the orbital period, so the angular momentum is extracted from the orbit, causing it to shrink. For reasons primarily related to the observed mass and period distributions of close white dwarf + main sequence binaries (e.g. Rappaport et al. 1983; Schreiber et al. 2010), it is often assumed that magnetic braking becomes inefficient below the fully convective boundary, corresponding roughly to $M \lesssim 0.35 M_{\odot}$.

It is tempting to attribute the lack of observed short-period BDs and low-mass stars to inefficient magnetic braking in fully-convective stars (e.g. Stepien 2006). It is worth remembering, however, that observational selection effects disfavor short-period binaries in magnitude-limited samples. The lack of detected short-period transiting BDs thus may simply reflect the fact that any main-sequence star or BD that can fit inside short-period orbits must necessarily be faint (e.g. El-Badry et al. 2022).

This paper presents the discovery of a BD in a binary with an orbital period much shorter than any such system discovered to date. The discovery was enabled by the Zwicky Transient Facility (ZTF; Bellm et al. 2019), which provides high-quality light curves for stars significantly fainter than other surveys that have been used to detect transiting BDs thus far. The remainder of the paper is organized as follows. Section 2 describes the object’s discovery and our follow-up photometric and spectroscopic observations. Section 3 presents our modeling of the system and a joint fit of its multi-band light curves, RVs, astrometry, and broadband SED. In Section 4, we compare the system to other known binaries containing BDs and discuss its formation history and future evolution. We summarize our results in Section 5.

2. DISCOVERY AND FOLLOW-UP OBSERVATIONS

We discovered ZTF J2020+5033 in the course of a search for low-mass eclipsing binaries described by El-Badry et al. (2022). That work applied the box least squares algorithm (Kovács et al. 2002) to ZTF light curves of main-sequence stars within ~ 500 pc of the Sun. The search identified 469 eclipsing binaries with extinction-corrected G -band absolute magnitudes $M_{G,0} > 10$, a limit that was chosen to select binaries in which both components are fully convective.

Visual inspection of the 469 light curves revealed ZTF J2020+5033 to be unique in that its optical light curves show a strong primary eclipse but no secondary eclipse. This implied that one component was much cooler than the other. Given that the unresolved source falls near the bottom of the main sequence and the primary is already quite cool (Figure 1), this suggested that the companion might be a BD, prompting our follow-up observations.

Basic observables of the system are shown in Figure 1, and its parameters are summarized in Table 1. The unresolved source has apparent magnitude $G = 18.7$, absolute magnitude $M_G = 12.92$, and colors $G - G_{\text{RP}} = 1.30$ and $G_{\text{BP}} - G_{\text{RP}} = 3.37$. The *Gaia* parallax implies a distance

of 142.7 ± 3 pc and places the source on the lower main sequence, well below the fully convective boundary. Assuming only one component contributes significantly to the optical photometry, the observed color and absolute magnitude imply a spectral type between M5 and M6 (e.g. Gaia Collaboration et al. 2021b). Unlike most of the eclipsing binaries in the El-Badry et al. (2022) sample, the source is not above the main sequence in the color-magnitude diagram. The parameters that we infer from light curve modeling (Section 3) imply that the M dwarf dominates in the optical, but the BD contributes $\approx 10\%$ of the light in the infrared; their separate and combined spectral energy distributions are shown in the right panel of Figure 1.

2.1. Light curves

2.1.1. ZTF

We analyzed the source’s ZTF DR17 light curves, which contain 881 clean epochs (i.e., `catflags` = 0) in the r -band and 141 in the g -band. The g -band data is noisy since the source is quite red, so we focus our analysis on the r -band data. The light curve spans 4.7 years (≈ 21600 orbits), with 30s exposures and a median uncertainty of 0.07 mag.

The orbital period, $P_{\text{orb}} \approx 1.90$ hr, was first estimated from the box-least-squares periodogram and then refined by fitting a light curve model (section 2.1.4). In addition to an obvious primary eclipse, the phased r -band light curve shows sinusoidal modulation on half the orbital period (Figure 2). We attribute this to tidal deformation of the M dwarf, allowing us to rule out a scenario where the period is 3.8 hours and the primary and secondary eclipses have similar depths.

2.1.2. CHIMERA

We observed ZTF J2020+5033 for a full orbit on 2022 August 25 with the Caltech High-speed Multi-color camera (CHIMERA; Harding et al. 2016). We observed in the Sloan g - and z_s -bands simultaneously, using 5 second exposures with ≈ 0.5 second gaps between frames. Both light curves are shown in Figure 2. The signal-to-noise ratio (SNR) of the z_s -band data is much higher than that of the g -band data. The primary eclipse is slightly deeper in the g -band. Ellipsoidal variation and hints of a secondary eclipse are evident in the z_s -band data.

2.1.3. WISE

ZTF J2020+5033 has been observed regularly by the *WISE* satellite (Wright et al. 2010; Mainzer et al. 2014). We retrieved the NEOWISE light curve from IRSA/IRPAC, restricting our analysis to data with `qual_frame` > 0. This yielded 208 usable measurements in the $W1$ ($3.4 \mu\text{m}$) and $W2$ ($4.6 \mu\text{m}$) bands. The light curve spans more than 8 years, with groups of 10-15 observations every ~ 6 months and exposures within each group typically separated by a few hours, resulting in fairly uniform phase coverage.

The *WISE* light curves are shown in the bottom two panels of Figure 2. Unlike in the optical data, there is clear evidence of a secondary eclipse at phase 0.5. This suggests that the secondary contributes a significant fraction of the total light in the infrared, but not in the optical, as expected if it has a comparable radius to the primary but a cooler temperature.

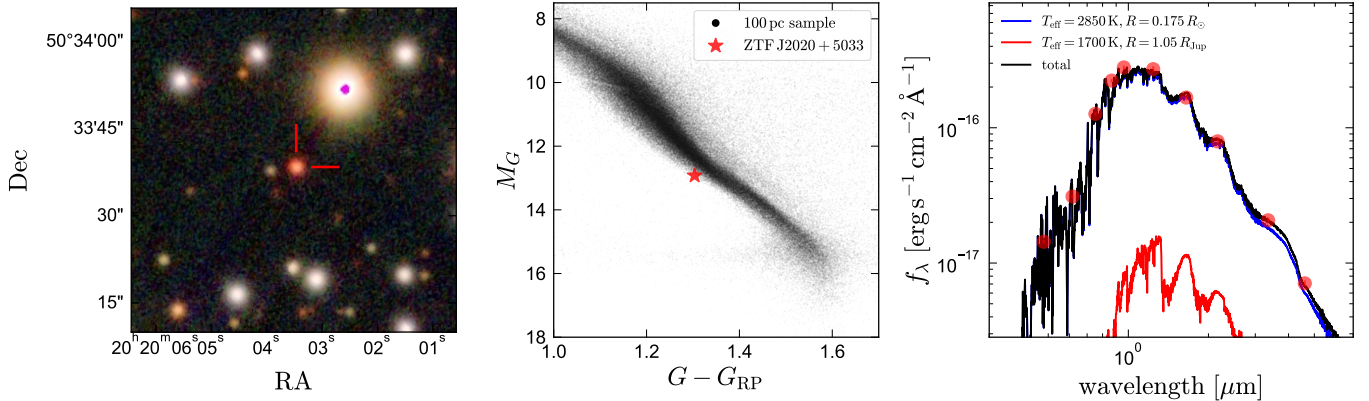


FIG. 1.— Left: 1-arcminute wide Pan-STARRS $i/r/g$ postage stamp centered on ZTF J2020+5033. Middle: the source’s position on the *Gaia* color-magnitude diagram, compared to the 100 pc sample. The source is slightly blueward of the main sequence, suggesting low metallicity and little contribution from a second star in the optical. Right: optical and infrared spectral energy distribution (SED), with best-fit models (Section 3) overplotted. The SED is dominated by an M dwarf with $T_{\text{eff}} \approx 2850$ K and $R \approx 0.175 R_{\odot}$. In the infrared, the cooler brown dwarf contributes $\approx 10\%$ of the light.

2.1.4. Photometric ephemeris

We fit the ZTF r -band light curve to determine a precise ephemeris as follows. We construct a light curve model for the r -band light curve using `e11c` (Maxted 2016) and the parameters inferred in Section 3. Treating P_{orb} and t_0 as free parameters, we predict the phase of each measurement and the corresponding predicted flux at that phase. We sample from the posteriors of P_{orb} and t_0 using `emcee` (Foreman-Mackey et al. 2013), employing flat priors and a likelihood that compares the predicted and measured normalized fluxes, assuming Gaussian uncertainties. We choose the orbital cycle on which t_0 is constrained to coincide with the ESI spectroscopic observations and adopt a convention where t_0 corresponds to the primary eclipse (i.e., BD in front of M dwarf).

The resulting constraints on P_{orb} and t_0 are reported in Table 1. The orbital period, $P_{\text{orb}} = 6850.1653 \pm 0.0014$ seconds, or $1.90282368 \pm 0.00000038$ hours, is constrained to 2 parts in 10^7 . This in principle allows the phase to be predicted with 1% accuracy within ± 10 years of t_0 . However, we caution that many close binaries undergo orbital period modulations due to magnetic activity in the component stars (Applegate 1992; Lanza et al. 1998), and the CHIMERA light curve suggests that such variations indeed occur in ZTF J2020+5033 (Section 2.1.5). The predictive power of the ephemeris is thus likely somewhat lower than the formal uncertainties suggest.

2.1.5. Evidence of transit timing variations

When we phased the CHIMERA data to the ephemeris inferred from the ZTF light curve, we found that the primary eclipse occurred 45 ± 3 seconds later than expected. This delay, while small, is quite significant, and the light curve fit is visibly poor if it is not accounted for. The simplest explanation is that the binary undergoes orbital period modulations resulting from magnetic activity-driven fluctuations in the components’ quadrupole moments, as is common in close binaries (e.g. Applegate 1992; Lanza et al. 1998; Watson & Marsh 2010).

It is also possible that the delay is a result of changes in light travel time due to the orbit of the binary around an unseen tertiary. In this case, a 45 second delay would correspond to a displacement of the binary by 0.09 au

along the line of sight. There are no nearby resolved *Gaia* sources whose parallaxes and proper motions are consistent with being bound to ZTF J2020+5033 (El-Badry et al. 2021). Given the faintness of the source and lack of spectral contributions from another luminous source (Section 2.2), the only plausible companions would be BDs or circumbinary planets. Such companions cannot be excluded, but given the frequent occurrence of timing variations in close binaries due to magnetic activity, the observed delay does not in itself provide strong evidence for a third body.

2.2. Phase-resolved spectroscopy

We observed ZTF J2020+5033 for ~ 2 hours on 2022 June 3 with the Echelle Spectrograph and Imager (ESI; Sheinis et al. 2002) on the 10 m Keck-II telescope on Maunakea. We used the $0.75''$ slit and 2×1 binning, yielding a resolution $R \approx 5500$, with wavelength coverage of 3900–10,000 Å. We reduced the data using the MAuna Kea Echelle Extraction (MAKEE) pipeline, which performs bias subtraction, flat fielding, wavelength calibration, and sky subtraction. We obtained 19 exposures, each with exposure time 300 seconds, and a 54 second gap between exposures for read-out (Table 2).

We flux-calibrated and merged spectra from individual orders using observations of a flux standard taken the same night. Small shifts in the wavelength solution were corrected by fitting the telluric absorption lines with a HITRAN model (Rothman et al. 2009; Gullikson et al. 2014); the inferred shifts were always within ± 2 km s $^{-1}$ of 0. To correct for slit losses and atmospheric dispersion, we fit a first-order polynomial correction to the flux calibration by requiring that the orbit-averaged coadded spectrum is consistent with the Pan-STARRS photometry.

Cutouts of the phased spectra are shown in the top panels of Figure 3. All the photospheric lines vary sinusoidally, as expected for a single-lined binary. There is no evidence of a second luminous component moving in anti-phase. $H\alpha$ and $H\beta$ are both observed in emission; this is most likely a result of chromospheric activity in the rapidly-rotating M dwarf (e.g. Newton et al. 2017).

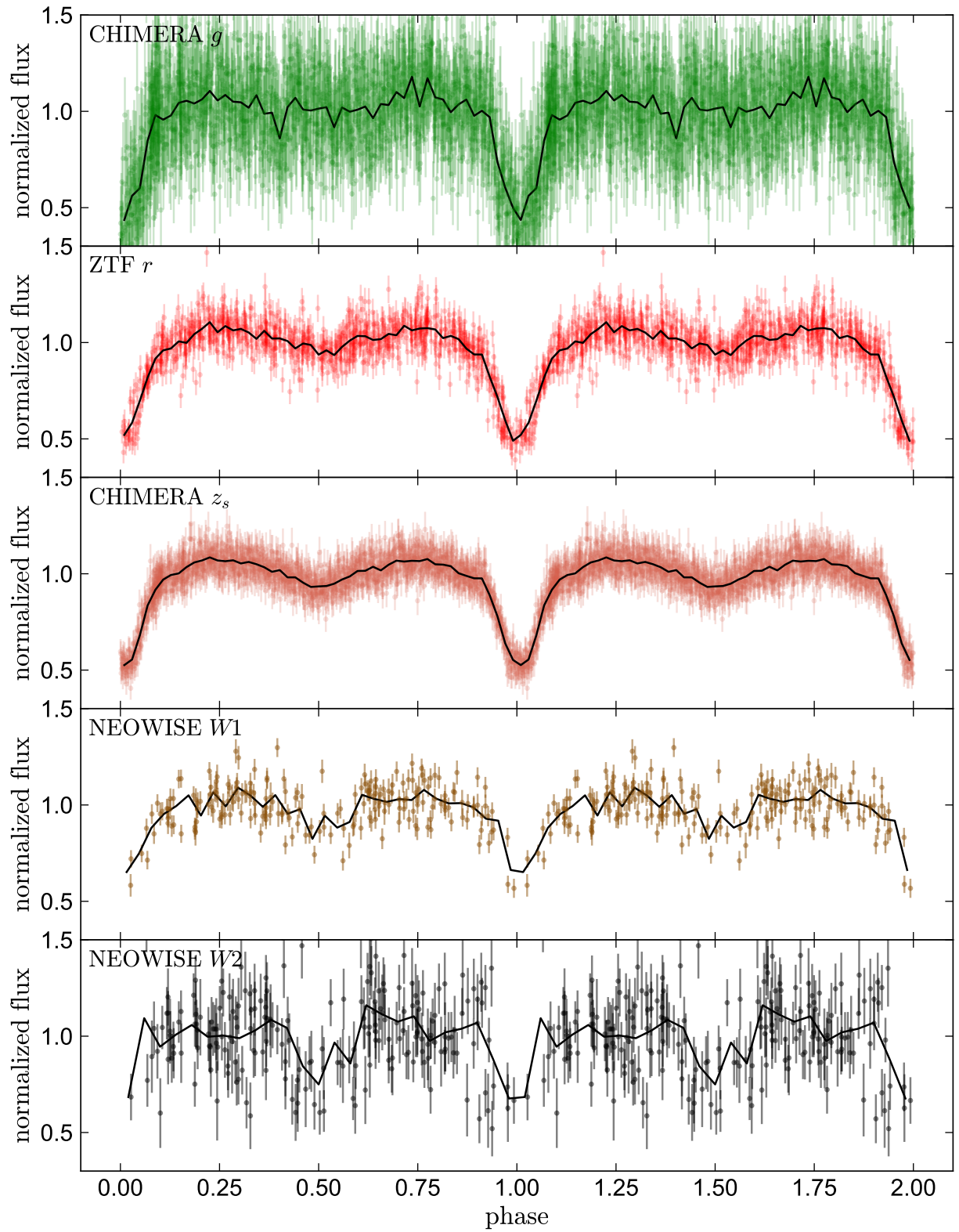


FIG. 2.— Phased light curves of ZTF J2020+5033 in five different bandpasses, with wavelength increasing from top to bottom. In the optical, there is a deep primary eclipse but no secondary eclipse, indicating that the secondary is much cooler than the primary. Secondary eclipses become evident in the infrared, where the cool secondary contributes a significant fraction of the total light. This constrains the secondary temperature (Figure 5).

2.2.1. Radial velocities

We measured RVs for the M dwarf by cross-correlating the normalized, tellurics-corrected spectra with a `BT-Settl` model spectrum (Allard et al. 2011). We used a solar-metallicity model with $T_{\text{eff}} = 2900\text{ K}$ and $\log [(g/\text{cm s}^{-1})] = 5$, consistent with our fitting of the spectrum and SED (Sections 2.2.3 and 3).

Most of the lines in the observed spectrum are broad and not well suited for measuring RVs. After some experimentation, we chose two separate spectral windows for RV measurements: the region between 8160 and 8220 Å, which includes the Na I $\lambda\lambda 8183, 8195$ doublet, and the region between 7655 and 7725 Å, which includes the K I $\lambda\lambda 7665, 7699$ doublet. These two regions are shown in the center middle and right panels of Figure 3. We pseudo-continuum normalized both the observed and model spectra by dividing by a running median in a 100 Å window. The Na I doublet appears in two separate ESI orders, which we analyze separately. For each window and exposure, we determine the RV that minimizes χ^2 , and estimate the uncertainty as the RV shift that corresponds to a χ^2 increase of 1. Finally, we report the inverse variance-weighted average of the RVs from the three windows. The RVs are reported in Table 2.

The bottom panel of Figure 3 shows the measured RVs. At most phases, they are well-described by a sinusoid with RV semi-amplitude $K = 107.8 \pm 1.2\text{ km s}^{-1}$, corresponding to a mass function $f(M_2) = 0.0103 \pm 0.0003 M_{\odot}$. However, there is a clear discontinuity at phase 1, which is also visible in the trailed spectra. This is a Rossiter-McLaughlin (RM) effect (Rossiter 1924; McLaughlin 1924), reflecting the fact that the BD first eclipses the blueshifted side of the rotating M dwarf, and later the redshifted side.

2.2.2. Projected rotation velocity

We constrain the projected rotation velocity, $v \sin i$, of the M dwarf from the broadening of the Na I $\lambda\lambda 8183, 8195$ doublet. To minimize orbital smearing and biases resulting from the RM effect, we only consider the 7 ESI exposures taken near conjunction (i.e., $|\phi - 0.25| < 0.09$ and $|\phi - 0.75| < 0.09$). We verified using simulations that the expected bias in $v \sin i$ due to orbital smearing in these exposures is $\lesssim 3\text{ km s}^{-1}$. We corrected these exposures for telluric absorption, co-added them in their rest frame, and compared the resulting spectrum to a grid of `BT-Settl` models with a range of $v \sin i$ values. This yielded a projected rotation velocity $v \sin i = 118 \pm 6\text{ km s}^{-1}$ for the M dwarf.

Our joint modeling of the light curve, RVs, and SED (Section 3) predicts $v \sin i = 2\pi R_{\star} \sin i / P_{\text{orb}} = 111.7 \pm 1.2\text{ km s}^{-1}$ if the M dwarf is tidally synchronized, consistent with this measurement.

2.2.3. Spectral type

We compared the flux-calibrated, coadded ESI spectrum to a grid of empirical spectral models created by Kesseli et al. (2017). That work produced high-SNR templates for each spectral subtype in the MK system by coadding SDSS/BOSS spectra of bright stars with that subtype. Spectral subtypes for stars in the library were assigned using the automated ‘‘Hammer’’ classification scheme described by Covey et al. (2007).

We compare the three closest-matching templates to the coadded rest-frame spectrum of ZTF J2020+5033 in Figure 4. As expected, the best-fitting templates are for dwarf stars with mid- to late-M spectral types. The M5 template clearly has an earlier spectral type than ZTF J2020+5033 : it is bluer and has shallower absorption features at red wavelengths. The M6 template is a reasonably good match in both broad spectral shape and in the strength of individual lines, though it slightly over-predicts the flux at bluer wavelengths. The M7 template is redder than the observed spectrum.

2.3. Spectral energy distribution

We constructed the broadband spectral energy distribution (SED) of ZTF J2020+5033 by combining photometry from the Pan-STARRS (DR2; Kaiser et al. 2002), 2MASS (Skrutskie et al. 2006), and WISE (Wright et al. 2010) surveys. The Pan-STARRS and WISE magnitudes are mean values calculated from 10+ epochs and thus represent the source’s time-averaged flux. The 2MASS magnitudes were measured in a single exposure at JD 2450994.9554, 24 years prior to t_0 , making it impractical to measure their phases reliably in the presence of period modulations (Section 2.1.5). The fact that our SED model reproduces the photometry from all surveys without significant systematics suggests that the 2MASS observations did not occur during the primary eclipse. The SED and best-fit model are shown in the right panel of Figure 1; mock photometry for both components is shown in the bottom right panel of Figure 5.

2.3.1. Primary mass from K_s -band absolute magnitude

The measured K_s -band magnitude of the binary is $K_s = 14.33 \pm 0.06$, corresponding to an absolute magnitude $M_{K_s} = 8.56 \pm 0.07$ at the distance inferred from the *Gaia* parallax. Our light curve fit implies that the BD contributes about 10% of the flux in the K_s -band, so the M dwarf has an absolute magnitude $M_{K_s} = 8.66 \pm 0.07$. The empirical $M_{K_s} - M_{\star}$ relation constructed by Mann et al. (2019) then predicts $M_{\star} = 0.132 \pm 0.005 M_{\odot}$, where the uncertainty accounts for both intrinsic scatter in the relation and uncertainty in M_{K_s} . This mass is on the high end of values predicted for an M6 spectral type (e.g. Baraffe & Chabrier 1996), which range from 0.10 to $0.13 M_{\odot}$, depending on the adopted conversion between color and spectral type.

2.3.2. Metallicity

We estimated the metallicity of the M dwarf using the empirical calibration from Mann et al. (2013). In brief, we measured equivalent widths of several temperature- and metallicity-sensitive spectral features in the coadded and flux-calibrated ESI spectrum, defining the local pseudo-continuum for each feature with a first-order polynomial fit to predetermined regions on either side of each feature. Mann et al. (2013) calculated an empirical metallicity estimator as a function of these features (their Equation 11) using M dwarfs in wide binaries with FGK companions of known metallicity. Their relation yields $[M/H] = -0.44$ for ZTF J2020+5033, with an estimated uncertainty of ~ 0.1 dex.

2.4. Galactic orbit and kinematic age

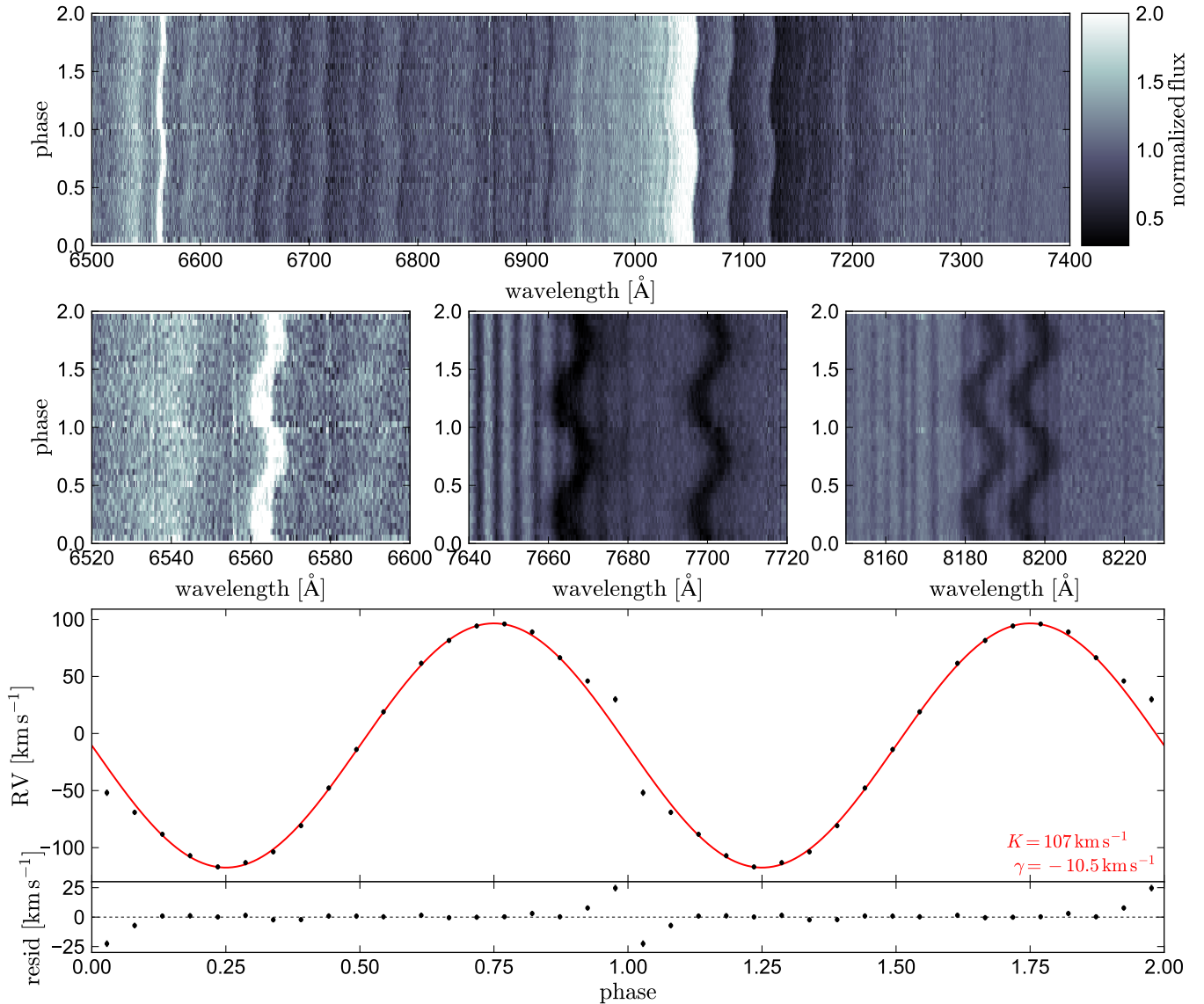


FIG. 3.— Phased ESI spectra of ZTF J2020+5033. Top panel shows a broad window spanning several orders; middle panels show cutouts of spectral regions including the H α line (left), the KI resonance doublet (middle) and the Na I doublet (right). In all panels, spectra are phased according to the photometric ephemeris and duplicated once. Stationary absorption lines are tellurics. There is no evidence of a second component moving in anti-phase of the primary. Bottom panel shows the measured RVs and best-fit sinusoid. The RVs are well-described by a sinusoid except during the primary eclipse (phase 1.0), when a clear Rossiter-McLaughlin effect is visible.

ZTF J2020+5033 has a tangential velocity relative to the Sun of $v_{\perp} = 4.74\mu/\varpi = 98 \text{ km s}^{-1}$, suggesting membership in an old and kinematically hot population. We calculated a Galactic orbit for the source using `galpy` (Bovy 2015). We used the parallax and proper motion from *Gaia* DR3 (Gaia Collaboration et al. 2021a, 2022), together with the center-of-mass RV inferred from the joint fit, as starting points to compute its orbit backward in time for 500 Myr. We used the Milky Way potential from McMillan (2017), but our results are only weakly sensitive to this choice. The orbit is characteristic of the thick disk, with moderate eccentricity and maximum excursions of ± 600 pc from the midplane. The current Galactocentric velocities in a cylindrical frame are $(v_R, v_{\phi}, v_z) = (-102, -228, +27) \text{ km s}^{-1}$. These velocities, particularly the large v_R , are significantly different from the local standard of rest and point towards the

source’s membership in a kinematically hot population.

While Galactic kinematics provide only rough constraints on stellar ages, the orbit of ZTF J2020+5033 rules out a young age. In the solar neighborhood, essentially no stars with ages below 5 Gyr have velocities in excess of 100 km s^{-1} with respect to the Sun (e.g. Seabroke & Gilmore 2007; Yu & Liu 2018). Even among stars older than 10 Gyr, a majority are slower than ZTF J2020+5033 (Sharma et al. 2014). We adopt a conservative lower limit of 5 Gyr for the system’s age.

3. PARAMETER INFERENCE

We constrain the masses, radii, and temperatures of both components, as well as the binary’s orbital inclination, with a joint fit of the measured RVs, CHIMERA and *WISE* light curves, the *Gaia* parallax, and the broadband SED. The role of each observable in constraining

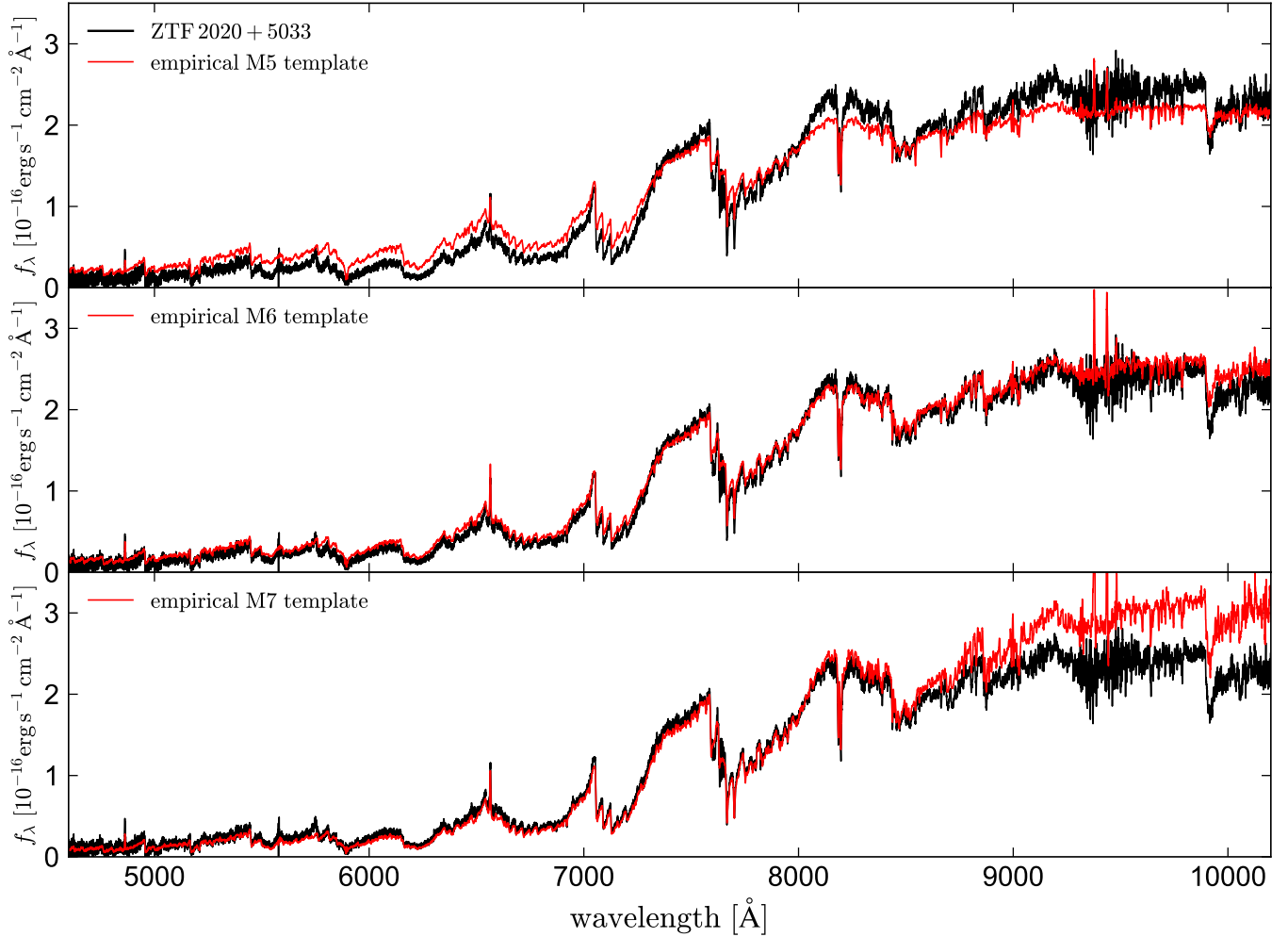


FIG. 4.— Coadded, rest-frame spectrum of ZTF J2020+5033 (black) compared to empirical templates for M dwarfs with a range of spectral types (red). All templates are scaled to match the observed flux at 8000 Å. The M5 template is bluer and has shallower spectra lines than the data, while the M7 template is redder. The M6 template provides the best match.

the system parameters is complex given the several overlapping constraints, but we summarize the most important constraints as follows.

1. The temperature and radius of the M dwarf are constrained by the SED and *Gaia* parallax.
2. The density of the M dwarf is constrained by the amplitude of ellipsoidal variations in the light curve, which are the result of its tidal deformation. Given the radius constraint from (1), this constrains the M dwarf’s mass.
3. The mass of the BD is constrained by the amplitude of the M dwarf’s RV variability, with a weak dependence on inclination.
4. The radius of the BD and the inclination are both constrained by the primary eclipse and by the observed RM effect.
5. The temperature of the BD is constrained by the depth of the secondary eclipse and its dependence on wavelength.

3.1. Light curve and RV models

We model the RVs and light curves in the g -, z_s , and $W1$ bands using `e11c` (Maxted 2016), a flexible code for calculating light curves and flux-weighted RVs of detached binaries. We use `e11c` rather than alternatives such as `PHOEBE` (Prša & Zwitter 2005) because it allows us to specify the surface brightness ratio – which we calculate using `BT-Settl` model SEDs – in each bandpass, which is more accurate than e.g. modeling the BD as a blackbody. Both components are modeled using the code’s `Roche` geometry. We take limb darkening and gravity darkening coefficients for each bandpass from Claret et al. (2012), using their 4-term parameterization for the limb darkening law. These authors did not calculate coefficients for the *WISE* $W1$ band, so we use their coefficients for the similar *Spitzer*/IRAC 3.6 μm band. We model reflection (i.e., heating of the BD’s “day” side by the M dwarf) using the simplified model described by Maxted (2016), leaving the albedo coefficient as a free parameter of the fit.

We calculate the surface brightness ratio of the two components in each band by integrating `BT-Settl` model

TABLE 1
Physical parameters and 1σ uncertainties for both components of ZTF J2020+5033.

Observables of the unresolved source		
Right ascension [J2016.0]	α [deg]	305.014397
Declination [J2016.0]	δ [deg]	50.560459
Apparent magnitude	G [mag]	18.70
Parallax	ϖ [mas]	7.05 ± 0.15
Proper motion (RA)	μ_α^* [mas yr $^{-1}$]	-105.02 ± 0.17
Proper motion (Dec)	μ_δ [mas yr $^{-1}$]	-100.21 ± 0.19
Tangential velocity	v_\perp [km s $^{-1}$]	97.6 ± 2.1
Extinction	$E(B - V)$ [mag]	0.0
Parameters of the M dwarf		
Effective temperature	$T_{\text{eff},*}$ [K]	2856 ± 6
Radius	R_* [R_\odot]	0.176 ± 0.002
Mass	M_* [M_\odot]	0.134 ± 0.004
Projected rotation velocity	$v_* \sin i$ [km s $^{-1}$]	118 ± 6
Surface gravity	$\log(g_*/(\text{cm s}^{-2}))$	5.07 ± 0.01
Bolometric luminosity	$\log(L_*/L_\odot)$	-2.73 ± 0.01
Parameters of the brown dwarf		
Effective temperature	$T_{\text{eff,BD}}$ [K]	1691 ± 127
Mass	M_{BD} [M_J]	80.1 ± 1.6
Radius	R_{BD} [R_J]	1.05 ± 0.01
Surface gravity	$\log(g_{\text{BD}}/(\text{cm s}^{-2}))$	5.25 ± 0.01
Bolometric luminosity	$\log(L_{\text{BD}}/L_\odot)$	-4.07 ± 0.12
Reflection parameter	α_{BD}	0.14 ± 0.07
Parameters of the binary		
Orbital period	P [day]	$0.07928432 \pm 0.000000016$
Conjunction time	t_0 [HJD UTC]	2459733.9125 ± 0.0002
M dwarf RV semi-amplitude	K_* [km s $^{-1}$]	107.8 ± 1.2
M dwarf center-of-mass velocity	γ_* [km s $^{-1}$]	-10.1 ± 0.6
Mass ratio	$q = M_{\text{BD}}/M_*$	0.571 ± 0.009
Orbital inclination	i [deg]	87.6 ± 1.6
Semimajor axis	a [R_\odot]	0.462 ± 0.004
Distance	d [pc]	136.4 ± 1.9
Age	τ [Gyr]	$5 - 13$
Gravitational wave inspiral time	t_{GW} [Gyr]	1.3 ± 0.1

JD UTC	phase	RV [km s $^{-1}$]	SNR
2459734.0405	0.61	61.5 ± 2.2	14.7
2459734.0446	0.67	81.5 ± 2.2	14.5
2459734.0487	0.72	94.2 ± 2.2	15.1
2459734.0528	0.77	96.0 ± 2.1	15.0
2459734.0569	0.82	89.0 ± 2.2	15.0
2459734.0610	0.87	66.4 ± 2.2	14.3
2459734.0651	0.92	46.0 ± 2.2	13.5
2459734.0692	0.98	29.9 ± 2.8	10.9
2459734.0733	0.03	-51.9 ± 2.8	11.0
2459734.0774	0.08	-69.1 ± 2.3	14.1
2459734.0815	0.13	-88.3 ± 2.2	15.4
2459734.0856	0.18	-107.1 ± 2.3	15.3
2459734.0897	0.23	-116.9 ± 2.2	15.6
2459734.0938	0.29	-113.2 ± 2.3	16.0
2459734.0979	0.34	-103.7 ± 2.2	15.4
2459734.1020	0.39	-80.8 ± 2.2	15.1
2459734.1061	0.44	-47.8 ± 2.3	14.6
2459734.1102	0.49	-14.0 ± 2.3	14.2
2459734.1142	0.54	19.0 ± 2.2	12.5

TABLE 2
Radial velocities from the ESI spectra. Timestamps are calculated at mid-exposure, and phases are calculated from the photometric ephemeris. SNR is calculated at 8200 Å.

spectra over the bandpass with `pyphot`.¹ We use the

¹ <https://mfouesneau.github.io/pyphot/>

Filter	system	central wavelength [μm]	mag
<i>g</i>	AB	0.48	21.27 ± 0.03
<i>r</i>	AB	0.62	19.90 ± 0.06
<i>i</i>	AB	0.75	17.95 ± 0.03
<i>z</i>	AB	0.87	17.03 ± 0.03
<i>y</i>	AB	0.96	16.56 ± 0.03
<i>J</i>	Vega	1.24	15.15 ± 0.05
<i>H</i>	Vega	1.65	14.58 ± 0.04
<i>K_s</i>	Vega	2.17	14.33 ± 0.06
<i>W₁</i>	Vega	3.35	14.00 ± 0.05
<i>W₂</i>	Vega	4.60	13.84 ± 0.05

TABLE 3
Spectral energy distribution. We adopt an uncertainty floor of 0.03 mag in all filters.

same process to calculate phase-averaged mean magnitudes of both components for comparison with the observed SED.

To model the RVs and RM effect, we first calculate the instantaneous RV curve, with the RV of each element of the M dwarf's surface weighted by that element's flux at 8200 Å. To account for finite exposure times, we then calculate a flux-weighted average over the 300-second exposure time of the ESI spectra.

3.2. Joint fit

We use a likelihood function that combines constraints from RVs, light curves, the SED, and astrometry:

$$\ln L = \ln L_{\text{RVs}} + \ln L_{\text{light curves}} + \ln L_{\text{SED}} + \ln L_{\text{ast}}. \quad (1)$$

Here $\ln L_{\text{RVs}}$ compares the predicted and measured RVs:

$$\ln L_{\text{RVs}} = -\frac{1}{2} \sum_i^{N_{\text{RVs}}} \frac{(\text{RV}_{\text{pred}}(t_i) - \text{RV}_i)^2}{\sigma_{\text{RV},i}^2}, \quad (2)$$

where RV_i are the RVs measured at times t_i , $\sigma_{\text{RV},i}$ are their uncertainties, and $\text{RV}_{\text{pred}}(t_i)$ are the exposure-averaged RVs predicted by `ellc`.

Similarly, $\ln L_{\text{light curves}}$ compares the predicted and observed light curves:

$$\ln L_{\text{light curves}} = -\frac{1}{2} \sum_{\lambda}^{N_{\text{bands}}} \sum_i^{N_{\text{epochs}}} \frac{(\hat{f}_{\lambda,\text{pred}}(t_i) - \hat{f}_{\lambda,i})^2}{\sigma_{\hat{f}_{\lambda,i}}^2}, \quad (3)$$

where $\hat{f}_{\lambda,i}$ represents the i th measurement of normalized flux in the λ th band, $\sigma_{\hat{f}_{\lambda,i}}$ is its uncertainty, and $\hat{f}_{\lambda,\text{pred}}(t_i)$ is the corresponding quantity predicted by `ellc`. The inner summation is over all photometric points in a given light curve and the outer summation is over the three different bandpasses.

$\ln L_{\text{SED}}$ compares the observed and predicted SED:

$$\ln L_{\text{SED}} = -\frac{1}{2} \sum_{\lambda} \frac{(m_{\text{pred},\lambda} - m_{\lambda})^2}{\sigma_{m_{\lambda}}^2}, \quad (4)$$

where m_{λ} and $\sigma_{m_{\lambda}}$ are the observed magnitudes of the source in different bandpasses and their corresponding uncertainties, and $m_{\text{pred},\lambda}$ are the predicted magnitudes of the unresolved source in each bandpass. We calculate $m_{\text{pred},\lambda}$ by interpolating on a grid of `BT-Sett1` model spectra, summing the predicted flux from the M dwarf and brown dwarf, and using `pyphot` to compute bandpass-averaged magnitudes.

Finally, $\ln L_{\text{ast}}$ compares the observed and predicted parallaxes:

$$\ln L_{\text{ast}} = -\frac{1}{2} \frac{(1/d - \varpi)^2}{\sigma_{\varpi}^2}, \quad (5)$$

where d is the distance in kpc, ϖ is the zeropoint-corrected *Gaia* parallax, and σ_{ϖ} is its uncertainty.

We adopt flat priors on all parameters except the M dwarf’s mass, for which we use a Gaussian prior $M_{\star} [M_{\odot}] \sim \mathcal{N}(0.0132, 0.005)$ that is motivated by the empirical $M_{K_s} - M_{\star}$ relation (Section 2.3.1). We sample from the posterior using `emcee` (Foreman-Mackey et al. 2013) using 64 walkers and taking 1000 steps after an initial 1000-step burn-in period.

3.3. Results

Figure 5 compares the predicted light curves, RVs, and SED to the observed data. The fit is in general quite good, with no obvious systematic differences between the model predictions and data. Joint constraints on several of the free parameters are shown in Figure 6 and reported in Table 1. Several parameters are covariant, as expected:

- R_{\star} and d are covariant because both rescale the predicted SED.
- R_{\star} and M_{\star} are covariant because the observed ellipsoidal variation constrains M_{\star}/R_{\star}^3 .
- M_{\star} and M_{BD} are covariant because the M dwarf’s predicted RVs increase with M_{BD} and decrease with M_{\star} .
- R_{BD} and R_{\star} are covariant because their ratio sets the primary eclipse depth.

These joint covariances also lead to covariances between parameters that are not obviously physically covariant, such as M_{BD} and R_{\star} . The constraint on the temperature of the BD is bimodal, with a dominant mode at $T_{\text{eff, BD}} \approx 1600$ K and a second mode at $T_{\text{eff, BD}} \approx 1850$ K. This occurs because the `BT-Sett1` model spectra predict the z_s -band flux to vary non-monotonically with T_{eff} , with slightly lower predicted flux (and thus, a shallower secondary eclipse) at 1700 K than at 1600 or 1800 K.

The best-fit mass of the M dwarf is $M_{\star} = 0.134 \pm 0.004 M_{\odot}$, which is 0.5σ above the prior from the Mann et al. (2019) relation. Since we have not measured RVs for the BD, the main constraint on M_{\star} comes from the amplitude of ellipsoidal variation in the light curve, and from the prior. The inferred mass of the BD is $M_{\text{BD}} = 80.1 \pm 1.6 M_{\text{J}}$, almost exactly equal to the theoretically expected hydrogen burning limit. This result is only weakly sensitive to varying the mass of the M dwarf within its uncertainties: if the mass of the M dwarf were $0.132 M_{\odot}$ (the central value of the prior as informed by the K_s -band absolute magnitude), the RVs would imply $M_{\text{BD}} = 79.2 M_{\text{J}}$ – still very close to the hydrogen burning limit.

The boundary between BDs and low-mass stars is near $\approx 80 M_{\text{J}}$, with some dependence on metallicity (Burrows et al. 1993; Baraffe et al. 2002; Dieterich et al. 2014; Baraffe et al. 2015), so our inferred M_{BD} is consistent with either a high-mass BD or a very low-mass star. However, the inferred temperature of the BD, $T_{\text{eff, BD}} = 1691 \pm 126$ K, is cooler than both theoretical (Section 4.1) and empirical (e.g. Dieterich et al. 2014) constraints on the minimum temperature of main-sequence stars, leading us to interpret the object as a probable BD.

4. DISCUSSION

4.1. Comparison to evolutionary models

Figure 7 compares our constraints on the temperature and radius of the BD to solar-metallicity ATMO 2020 evolutionary models for BDs (Phillips et al. 2020) and very low-mass star models from Baraffe et al. (2015). We assume a minimum age of 5 Gyr, as motivated by the star’s thick disk-like Galactic orbit (Section 2.4). At this age, the observed temperature is consistent with the highest-mass BD models in the ATMO 2020 library, which have masses between 75 and 79 M_{J} . This is consistent with our dynamically-inferred mass.

On the other hand, the BD’s radius is significantly larger than the models predict. The 78.6 M_{J} model predicts a radius of $0.85 R_{\text{J}}$ at ages of > 5 Gyr, meaning that at $1.06 R_{\text{J}}$, the BD is $\approx 25\%$ larger than expected.

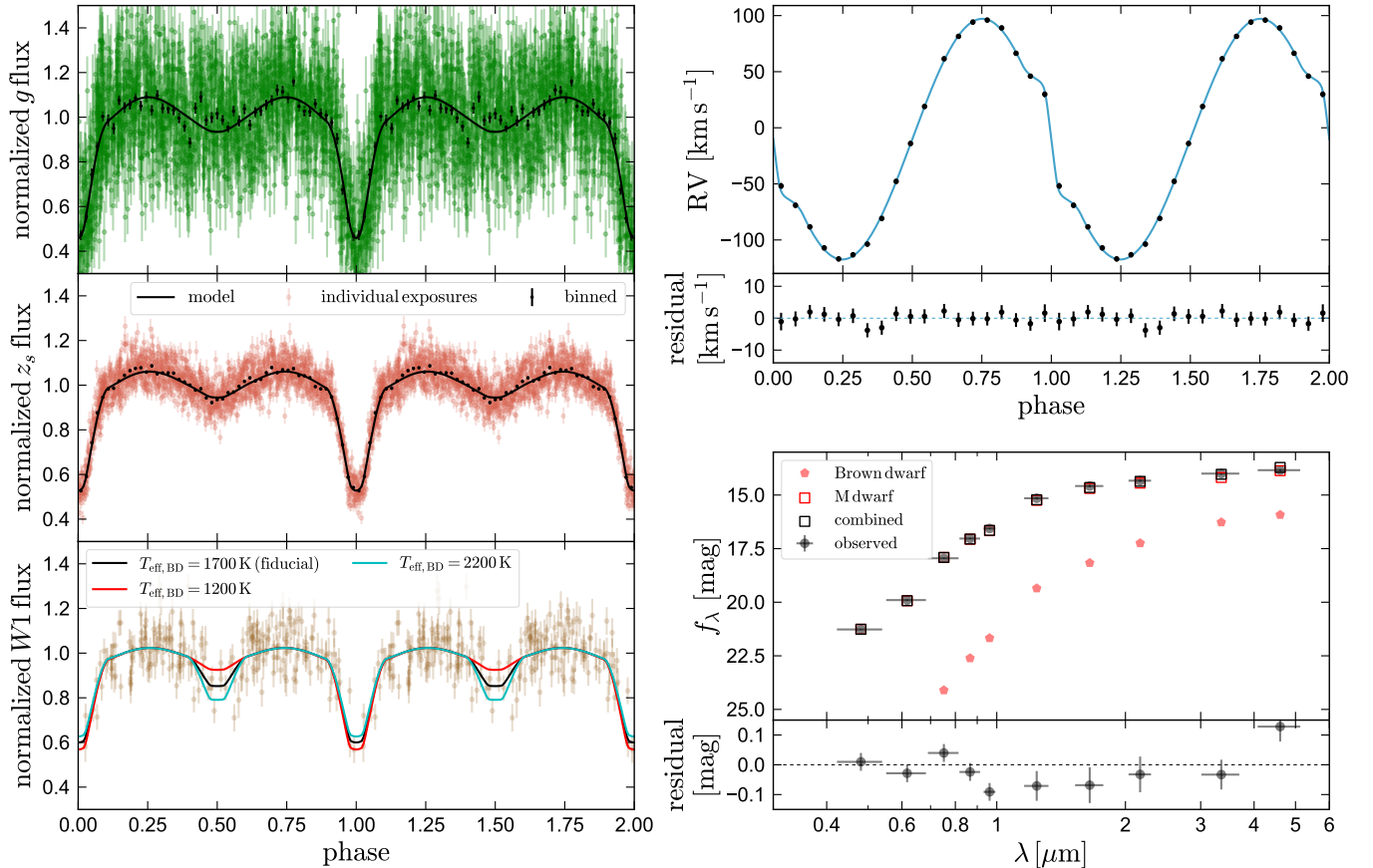


FIG. 5.— Posterior predictive checks for joint fitting of light curves, RVs, and the SED. Left panel shows the best-fit `e11c` light curves, compared to the observed light curves in the g , z_s , and $W1$ bands. Black points in the upper left and center panels show binned averages of the data. Bottom left panel shows how the secondary eclipse in the $W1$ band constrains the temperature of the BD. Upper right panel shows the predicted instantaneous RV curve; the residuals account for the finite exposure time of the observed RVs. Bottom right shows the fit to the SED, with the contributions from the two components shown separately. The fit is successful in matching all observables without obvious systematics.

The model matches the observed radius only at an age of 400 Myr, which is implausibly young given the system’s kinematics (Section 2.4). This implies that the BD is inflated.

We also compared to the BD’s parameters to the Sonora evolutionary models from Marley et al. (2021), assuming a metallicity $[\text{Fe}/\text{H}] = -0.5$. This yielded results quite similar to those from the ATMO 2020 models: the BD’s temperature implies a mass of $76 - 79 M_J$ for ages of 5–10 Gyr, and the predicted radius of a non-inflated BD in this age range is $0.80 - 0.86 R_J$.

The M dwarf is also somewhat larger than predicted by evolutionary models, with a radius of $0.175 \pm 0.002 R_\odot$ at a mass where evolutionary models (e.g. Baraffe et al. 2015) predict a radius of $\approx 0.16 R_\odot$. This radius is, however, typical of observed M dwarfs in this mass range (e.g. Parsons et al. 2018).

4.2. Is the secondary a BD or a low-mass star?

The secondary mass we infer is very close to the hydrogen burning limit, raising the possibility that the object could be a low-mass star rather than a BD. Recent evolutionary calculations place the hydrogen burning limit at $\approx 78.5 M_J$ at solar metallicity (Chabrier et al. 2023), rising toward lower metallicities. The exact value of the limit is uncertain at the $\sim 0.02 M_J$ level due to uncer-

tainties in evolutionary models, particularly the equation of state. We thus cannot distinguish between star and BD secondaries on the basis of mass alone.

Even at old ages, models predict a smooth transition between the lowest-mass stars and highest-mass BDs, with the highest-mass BDs undergoing unsteady hydrogen burning that contributes a significant fraction of their luminosity even after 10 Gyr (Chabrier & Baraffe 1997; Zhang et al. 2017). We classify the secondary as a BD because it is cooler than the stellar/substellar boundary at ~ 2100 K empirically-inferred by Dieterich et al. (2014). Given the uncertainty in this limit and (e.g. Dupuy & Liu 2017), we cannot fully rule out the possibility that the secondary is a low-mass star, but we consider a BD more likely.

4.3. Comparison to other known BDs

Figure 8 compares ZTF J2020+5033 to 39 other transiting BDs whose masses, radii, and orbital periods were tabulated by Carmichael (2023). These systems represent a majority of the currently known transiting BD population. All of these host stars are the main sequence; BDs orbiting white dwarfs were not included. The most unusual property of the system compared to the known population is its orbital period, which is 7 times shorter than the previous record holder, TOI 263.01 (Parviainen

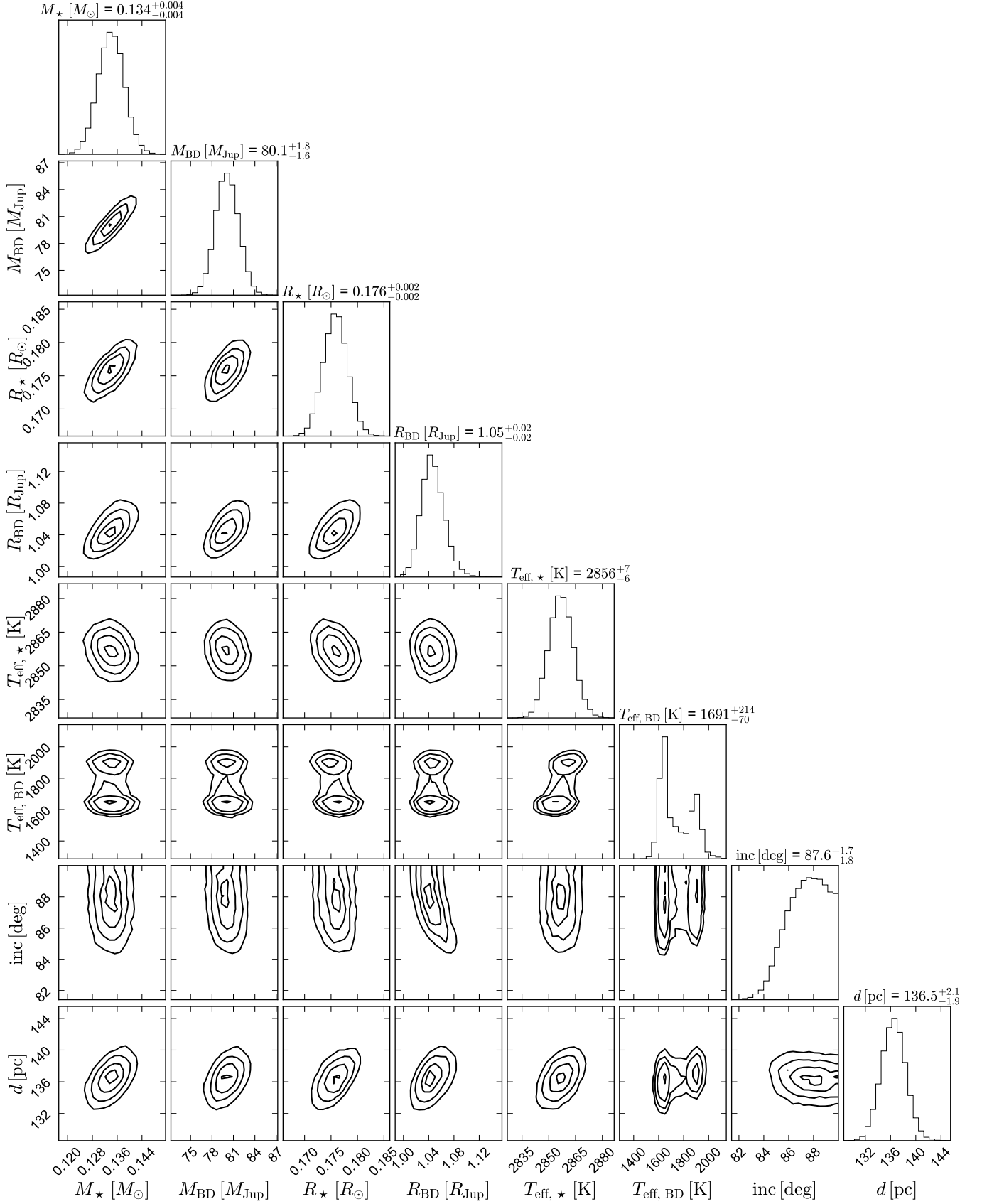


FIG. 6.— Constraints from joint fitting of light curves, RVs, and the broadband SED. Parameters with a “ \star ” subscript refer to the M dwarf, while those with the subscript “BD” refer to the brown dwarf. Masses, radii, and temperatures of both components are constrained with a precision of a few percent or better (see Table 1 for constraints on all parameters).

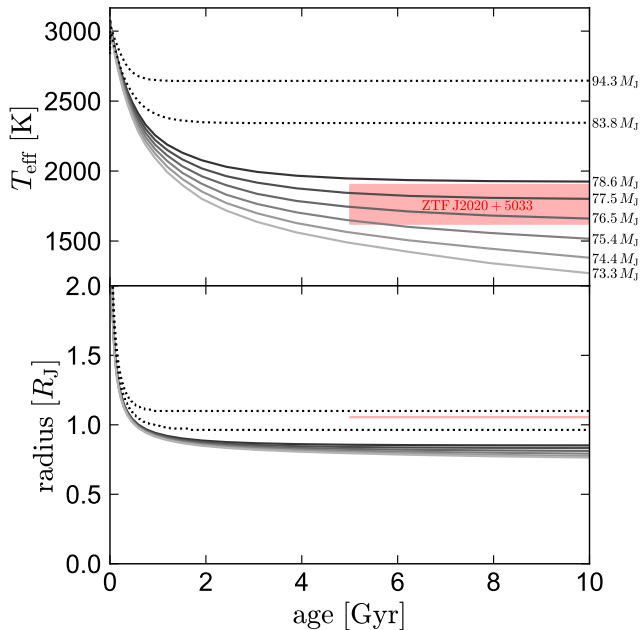


FIG. 7.— Temperature and radius of ZTF J2020+5033 compared to evolutionary models for massive brown dwarfs (solid lines) and very low-mass stars (dotted lines). Given the system’s old age (as constrained by its Galactic orbit), its effective temperature implies a mass of $76\text{--}78 M_J$. This is quite close to the dynamically-inferred mass of $80.1 \pm 1.7 M_J$, and *just* at the hydrogen burning limit. The measured radius is $\approx 25\%$ larger than predicted by evolutionary models.

et al. 2020; Palle et al. 2021). The shaded region in the left panel shows the boundary below which BDs with radii between 1.0 and $1.4 R_J$ would overflow their Roche lobes. The BD in ZTF J2020+5033 still falls comfortably within its Roche lobe ($R_{BD}/R_{\text{Roche lobe}} \approx 0.71$) but would overflow it if its radius were larger than $1.5 R_J$, or at its current radius if its mass were lower than $30 M_J$.

Most of the other BDs shown in Figure 8 transit solar-type stars, which are less dense than the M dwarf in ZTF J2020+5033. Solar-type stars with $80 M_J$ companions overflow their Roche lobes at $P_{\text{orb}} \lesssim 6$ hours (0.25 days). A period as short 1.9 hours can only occur around a low-mass main sequence star, BD, or compact object. Nevertheless, none of the other BDs shown in Figure 8 orbit stars that fill or nearly fill their Roche lobes, so the dearth of BDs with $P_{\text{orb}} \lesssim 1$ d is not (purely) a consequence of the Roche limit.

The secondary in ZTF J2020+5033 is among the most massive known BDs, assuming it indeed is a BD. The right panel of Figure 8 shows that the object’s radius is typical for the population of observed high-mass BDs. There are two other objects with similar masses and larger radii: TOI-587b, with $M = 79.9 \pm 5.3 M_J$ and $R = 1.38 \pm 0.04 R_J$ (Grievés et al. 2021), and NGTS-7Ab, with $M = 75.5 \pm 13.7 M_J$ and $R = 1.38 \pm 0.04 R_J$ (Jackman et al. 2019). However, both of these systems are known to be young, with respective inferred ages of 200 and 55 Myr. The object most similar to ZTF J2020+5033 is thus KOI-189b, with $M = 80.4 \pm 2.3 M_J$ and $R = 0.99 \pm 0.02 R_J$ (Díaz et al. 2014). That object has an inferred age of 6 Gyr and a radius 15% larger than expected from evolutionary models, comparable to ZTF J2020+5033. Díaz et al. (2014) attributed the infla-

tion of this object to inhibition of convection by strong magnetic fields (e.g. Mullan & MacDonald 2001). Such a scenario could plausibly also apply to ZTF J2020+5033, particularly given that tidal synchronization is expected to maintain a dynamo.

We consider tides or irradiation less likely to be responsible for the BD’s inflation, since there exist BDs that are more strongly irradiated and experience stronger tides and are not inflated (Littlefair et al. 2014; Parsons et al. 2017). One such case is the white dwarf + BD binary SDSS J1205-0242, which contains a BD with mass $51 M_J$ orbiting a hot WD ($T_{\text{eff}} = 23680 \pm 430$ K) in an orbital period of only 1.19 hours. The luminosity of the WD is $L_{\text{WD}} = 0.14 L_{\odot}$, 80 times brighter than the M dwarf in ZTF J2020+5033. The orbital separation is 5% smaller, leading to an incident flux per unit area ≈ 90 times higher than the flux on the BD in ZTF J2020+5033. The incident flux must have been even higher in the past, when the 50 Myr-old WD was younger and hotter. Yet, the BD in SDSS J1205-0242 is not inflated: with a radius of only $0.82 \pm 0.03 R_J$, it is one of the smallest known BDs. Some of the observed BDs orbiting solar-type stars with $P_{\text{orb}} = 1\text{--}3$ d also experience a higher incident flux than the BD in ZTF J2020+5033 on account of their much more luminous host stars (e.g. Sebastian et al. 2022). Given that the amount of radius inflation in other massive BDs is also not strongly correlated with how much they are irradiated, we conclude that it is more likely to be a result of processes internal to the BD.

About a dozen BDs are known that are in short-period detached binaries with white dwarf or hot subdwarf companions (e.g. Burleigh et al. 2006; Geier et al. 2011; Steele et al. 2013; Parsons et al. 2017; Casewell et al. 2018, 2020a,b), and several of these have orbital periods of 1-2 hours. The critical difference between these systems and ZTF J2020+5033 is that they are post-common envelope systems, meaning that the BD likely formed in wide orbit (\sim au) and only ended up at short periods after a common envelope event. There is no need to appeal to magnetic braking to explain the tight orbits of BDs in post-common envelope binaries. ZTF J2020+5033 has the shortest confirmed orbital period among all non-post common envelope binaries (whether they contain main-sequence stars or BDs; e.g. Nefs et al. 2012; Soszyński et al. 2015).

4.4. Formation history

The two components of ZTF J2020+5033 both currently fit inside their Roche lobes, but both must have been significantly larger in youth. For example, at an age of 1 Myr, the M dwarf is predicted to have had a radius of $1.2 R_{\odot}$ (e.g. Baraffe et al. 2015); at this age, it would have overflowed its Roche lobe for any $P_{\text{orb}} < 1.16$ days. At an age of 10 Myr, the same figures are $0.49 R_{\odot}$ and 0.31 days. The simplest explanation is thus that the binary formed with a wider orbit and subsequently shrunk via magnetic braking. Dynamical interactions with other bodies in the system’s birth environment and/or an unseen tertiary component likely also played an important role in the binary’s formation (Tokovinin et al. 2006), but such interactions become inefficient once tides dominate apsidal precession (e.g. Holman et al. 1997; Blaes et al. 2002; Fabrycky & Tremaine 2007). In the absence of magnetic braking or other sources of angular momen-

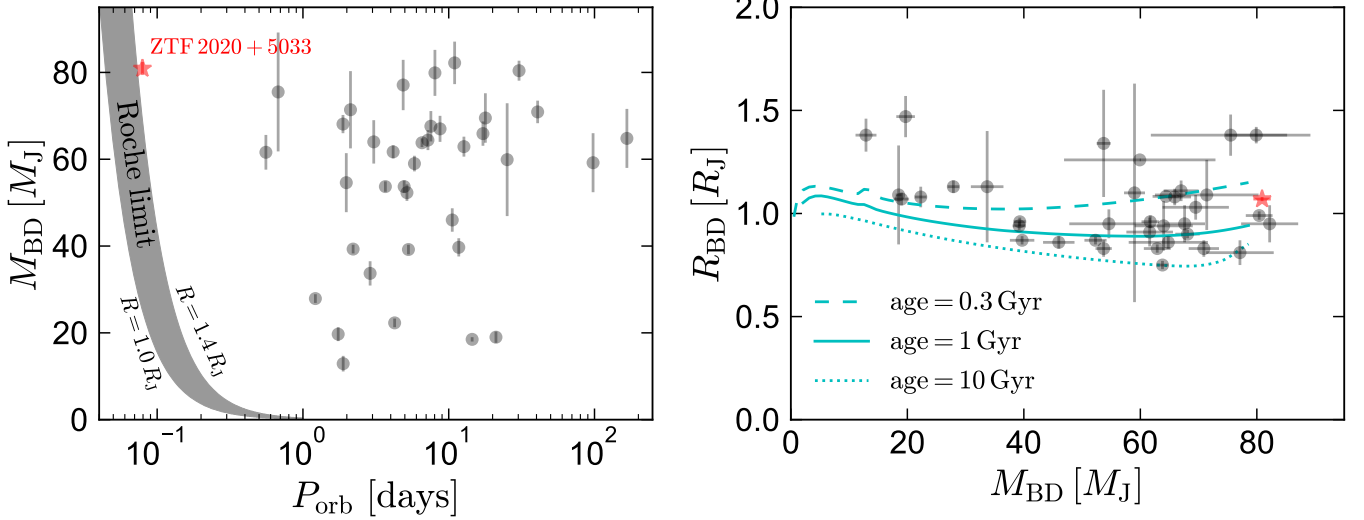


FIG. 8.— Comparison of ZTF J2020+5033 to other transiting BDs, as compiled by Carmichael (2023). Left: ZTF J2020+5033 has by far the shortest orbital period of known BDs orbiting stars, and one of the highest masses. BDs below the shaded region would overflow their Roche lobes; ZTF J2020+5033 is the only object near this limit. Right: masses and radii for the same systems shown in the left panel. Cyan lines show predictions from ATMO 2020 evolutionary models (Phillips et al. 2020) for three different ages. ZTF J2020+5033 has a radius similar to other observed high-mass BDs. However, its radius would be consistent with the ATMO 2020 models only at an age of order 400 Myr, which is much younger than implied by its Galactic orbit. This suggests the brown dwarf is somewhat inflated.

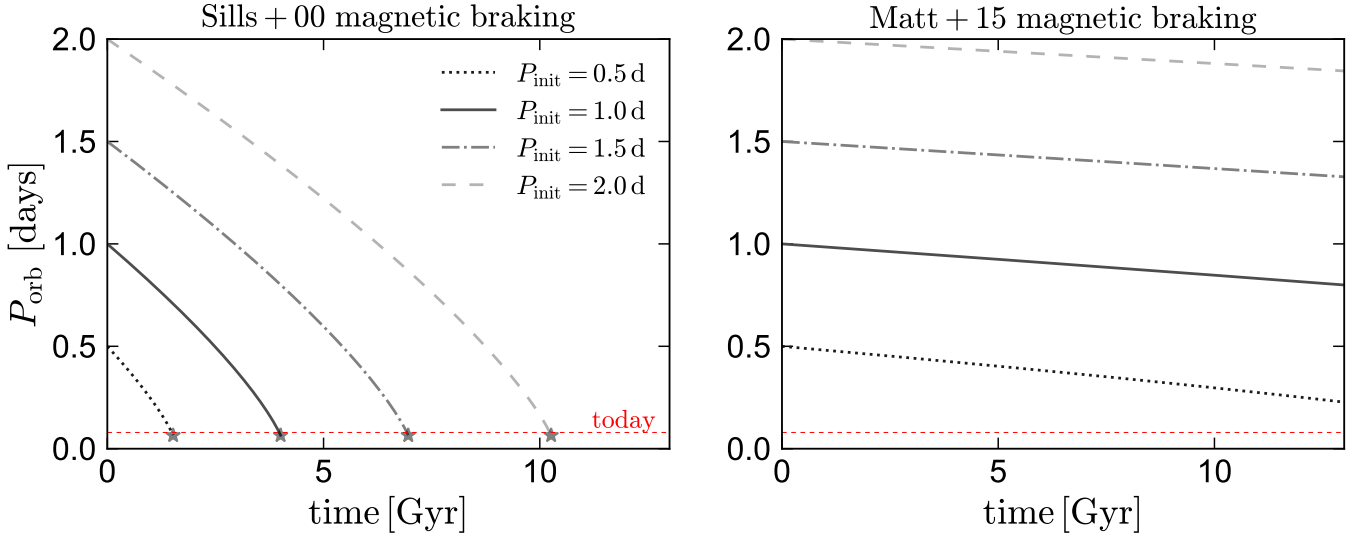


FIG. 9.— Predicted orbital period evolution of ZTF J2020+5033 under two different magnetic braking laws. In both panels, different tracks show four different initial periods, dashed red line shows the period of ZTF J2020+5033, and grey stars show the onset of mass transfer. With the Sills et al. (2000) prescription (left panel), magnetic braking is fairly efficient and can explain the current orbit for any initial period below 2 days. Matt et al. (2015, right panel) predicts significantly weaker magnetic braking and cannot significantly shrink the orbit in a Hubble time.

tum loss, we thus do not expect binary orbits to shrink below 1-2 days (e.g. Stepien 2006; Hwang & Zakamska 2020). Gravitational waves are too weak to explain the observed orbit: assuming an age of 10 Gyr, the initial period would have been only 0.14 days if they provided the only angular momentum loss (Peters 1964). This suggests that magnetic braking remains efficient in at least some fully-convective stars.

To assess how the orbit may have shrunk, we calculated its expected evolution under two different magnetic braking prescriptions. The first is taken from Sills et al. (2000), as motivated by Kawaler (1988) and Chaboyer et al. (1995), and the second from Matt et al.

(2015), based on the rotation period distributions of stars observed by *Kepler*. Both prescriptions place ZTF J2020+5033 in the saturated regime, with $\dot{J} \propto P_{\text{orb}}^{-1}$, but the calibration from Matt et al. (2015) declines more strongly at low masses and thus predicts weaker braking.

Figure 9 shows the predicted orbital evolution of ZTF J2020+5033 under both magnetic braking laws for four different initial periods. As described by El-Badry et al. (2022), we assume both components are tidally synchronized and that each component removes angular momentum from the orbit following the same (mass- and radius-dependent) braking law. Tracks terminate at an orbital

period of 1.56 hours, when the M dwarf will overflow its Roche lobe.

The Sills et al. (2000) magnetic braking prescription (left panel) predicts relatively efficient angular momentum loss, such that any initial period below 2 days could reach the observed orbit within 10 Gyr. In this prescription, magnetic braking dominates over gravitational waves at all periods, such that the inspiral time until Roche lobe overflow is predicted to be only 30 Myr, compared to the predicted 1.3 Gyr due to gravitational waves alone.

In contrast, the Matt et al. (2015) prescription (right panel) predicts magnetic braking to be rather weak, resulting in only small changes to the orbital period over a Hubble time. In this prescription the magnetic braking torque scales as $\dot{J}_{\text{MB}} \propto R^{3.1} M^{0.5}$, resulting in very weak braking for low-mass stars and BDs. With such weak braking it is impossible to explain the current orbit of ZTF J2020+5033 in the context of isolated binary evolution.

Given our conclusion that the orbit of ZTF J2020+5033 likely decayed due to magnetic braking, we can consider whether there exist plausible progenitor systems with wider orbits. The recently discovered binary LP 413-53AB – which was until now the shortest-period known binary containing a late M dwarf and a likely BD – is a prime candidate. That system has an orbital period of 17 hours and components similar to ZTF J2020+5033 (Hsu et al. 2023). Its orbit will likely continue to shrink via magnetic braking, which in the Sills et al. (2000) prescription will bring it to a period of 1.9 hours within a few Gyr.

4.5. Future evolution

Because the BD is somewhat more dense than the M dwarf, it is the M dwarf that will first overflow its Roche lobe. Given the M dwarf’s current radius, this will occur at an orbital period of 1.56 hours. The orbit is by now tight enough that gravitational wave-driven inspiral is important for the binary’s future evolution, despite the low masses of the two components. If the orbit decays *only* due to gravitational waves, the M dwarf will overflow its Roche lobe in 1.3 Gyr. This represents a lower limit on the system’s remaining lifetime as a detached binary, because magnetic braking likely contributes significant additional angular momentum loss.

When the M dwarf overflows its Roche lobe, the closest approach of the accretion stream to the BD is predicted to be $r_{\text{min}} \approx 0.15 R_{\text{J}}$ (Lubow & Shu 1975). Because this is smaller than the radius of the BD, mass transfer is predicted to occur through direct impact accretion rather than through a disk. This will lead to the formation of a hot spot on the BD, most likely leading to significant changes in the optical light curve.

The fate of ZTF J2020+5033 following the onset of mass transfer is somewhat uncertain. Given that $M_{\star} > M_{\text{BD}}$, mass transfer will at first proceed on the M dwarf’s thermal timescale, which is of order 1 Gyr. Since the BD’s thermal timescale is significantly longer than this, it may expand as a result of accretion, potentially resulting in the formation of a common-envelope and a long-lived contact binary. If the system survives, it would be a good candidate to form an ultramassive BD more massive than

the hydrogen burning limit (e.g. Salpeter 1992; Forbes & Loeb 2019).

There very likely exist analogs of ZTF J2020+5033 in which *both* components are BDs. Such systems would be very faint in the optical while detached, but might appear as high-amplitude variables in the optical due to their rotating hot spots once mass transfer begins. Indeed, several such sources have recently been discovered in ZTF data. Their properties and possible evolutionary link to detached binaries like ZTF J2020+5033 will be explored in future work.

4.6. Prospects for finding more short-period BDs

At a distance of only ≈ 140 pc, ZTF J2020+5033 is closer than 34 of the 39 other known transiting BDs shown in Figure 8. This suggests that BDs in short-period orbits are not particularly rare. However, ZTF J2020+5033 is almost 2 magnitudes fainter in the *G* band than any of those systems. This reflects the fact that the host star has a high density and low mass – as it must in order to fit inside a tight orbit. Most of the other known transiting BDs were discovered by surveys like *TESS Kepler*, *CoRoT*, and *WASP*, which have limited sensitivity to faint, low-mass stars. Deeper forthcoming surveys such as *WINTER* (Lourie et al. 2020), *Rubin* (Ivezić et al. 2019), and *Roman* (Spergel et al. 2015) thus have bright prospects for detecting more BDs in short-period orbits.

5. SUMMARY AND CONCLUSION

We have discovered a new detached binary containing a low-mass star ($M_{\star} = 0.134 \pm 0.004 M_{\odot}$; spectral type M6) and a high-mass BD ($M_{\text{BD}} = 80.1 \pm 1.6 M_{\text{J}}$; spectral type L5). Joint fitting of the system’s spectral energy distribution (Figures 1 and 4) multi-band light curves (Figure 2), and radial velocities (Figure 3) allow us to place tight constraint on the physical parameters of both components (Figures 5 and 6). We find that the BD is mildly inflated and has a mass just below the hydrogen burning limit (Figure 7).

With an orbital period of only 1.90 hours, the system is much more compact than other known transiting brown dwarfs (Figure 8). Both components must have been significantly larger when they were young than they are today, implying that the orbit has shrunk significantly by magnetic braking. This strongly suggests that magnetic braking remains efficient below the fully convective boundary in at least some stars (Figure 9), contrary to the common assumption in many binary evolution models.

The system’s orbit will continue to decay in the future, and the M dwarf will overflow its Roche lobe in 1.3 Gyr if gravitational radiation is the only significant angular momentum loss mechanism. In the likely event that magnetic braking leads to additional angular momentum loss, mass transfer is expected to begin within a few tens of Myr.

ACKNOWLEDGMENTS

We thank the anonymous referee for a constructive report, and Jackie Faherty, Mercedes López-Morales, and David Charbonneau for useful discussions.

Based on observations obtained with the Samuel Oschin Telescope 48-inch and the 60-inch Telescope at

the Palomar Observatory as part of the Zwicky Transient Facility project. ZTF is supported by the National Science Foundation under Grant No. AST-2034437 and a collaboration including Caltech, IPAC, the Weizmann Institute for Science, the Oskar Klein Center at Stockholm University, the University of Maryland, Deutsches Elektronen-Synchrotron and Humboldt University, the TANGO Consortium of Taiwan, the University of Wisconsin at Milwaukee, Trinity College Dublin, Lawrence Livermore National Laboratories, and IN2P3, France. Operations are conducted by COO, IPAC, and UW.

The data presented herein were obtained at the W. M. Keck Observatory, which is operated as a scientific partnership among the California Institute of Technology, the University of California and the National Aeronautics and Space Administration. The Observatory was made possible by the generous financial support of the W. M. Keck Foundation. The authors wish to recognize and acknowledge the very significant cultural role and reverence that the summit of Maunakea has always had within the indigenous Hawaiian community. We are most fortunate to have the opportunity to conduct observations from this mountain.

REFERENCES

- Acton J. S., et al., 2021, *MNRAS*, **505**, 2741
 Aganze C., et al., 2022, *ApJ*, **924**, 114
 Allard F., Homeier D., Freytag B., 2011, in Johns-Krull C., Browning M. K., West A. A., eds, *Astronomical Society of the Pacific Conference Series Vol. 448*, 16th Cambridge Workshop on Cool Stars, Stellar Systems, and the Sun. p. 91 ([arXiv:1011.5405](https://arxiv.org/abs/1011.5405)), doi:10.48550/arXiv.1011.5405
 Applegate J. H., 1992, *ApJ*, **385**, 621
 Baglin A., et al., 2006, in 36th COSPAR Scientific Assembly. p. 3749
 Baraffe I., Chabrier G., 1996, *ApJ*, **461**, L51
 Baraffe I., Chabrier G., Allard F., Hauschildt P. H., 2002, *A&A*, **382**, 563
 Baraffe I., Homeier D., Allard F., Chabrier G., 2015, *A&A*, **577**, A42
 Bayless A. J., Orosz J. A., 2006, *ApJ*, **651**, 1155
 Bellm E. C., et al., 2019, *PASP*, **131**, 018002
 Blaes O., Lee M. H., Socrates A., 2002, *ApJ*, **578**, 775
 Borucki W. J., et al., 2010, *Science*, **327**, 977
 Bouchy F., Deleuil M., Guillot T., Aigrain S., Carone L., Cochran W. D., 2010, *arXiv e-prints*, p. arXiv:1010.0179
 Bovy J., 2015, *ApJS*, **216**, 29
 Burleigh M. R., Hogan E., Dobbie P. D., Napiwotzki R., Maxted P. F. L., 2006, *MNRAS*, **373**, L55
 Burrows A., Hubbard W. B., Saumon D., Lunine J. I., 1993, *ApJ*, **406**, 158
 Carmichael T. W., 2023, *MNRAS*, **519**, 5177
 Carmichael T. W., et al., 2020, *AJ*, **160**, 53
 Casewell S. L., et al., 2018, *MNRAS*, **476**, 1405
 Casewell S. L., et al., 2020a, *MNRAS*, **497**, 3571
 Casewell S. L., et al., 2020b, *MNRAS*, **497**, 3571
 Casewell S. L., Debes J., Braker I. P., Cushing M. C., Mace G., Marley M. S., Kirkpatrick J. D., 2020c, *MNRAS*, **499**, 5318
 Chaboyer B., Demarque P., Pinsonneault M. H., 1995, *ApJ*, **441**, 876
 Chabrier G., Baraffe I., 1997, *A&A*, **327**, 1039
 Chabrier G., Baraffe I., Phillips M., Debras F., 2023, *A&A*, **671**, A119
 Claret A., Hauschildt P. H., Witte S., 2012, *A&A*, **546**, A14
 Covey K. R., et al., 2007, *AJ*, **134**, 2398
 Cruz P., Diaz M., Birkby J., Barrado D., Sipöcz B., Hodgkin S., 2018, *MNRAS*, **476**, 5253
 Díaz R. F., et al., 2014, *A&A*, **572**, A109
 Dieterich S. B., Henry T. J., Jao W.-C., Winters J. G., Hosey A. D., Riedel A. R., Subasavage J. P., 2014, *AJ*, **147**, 94
 Dupuy T. J., Liu M. C., 2017, *ApJS*, **231**, 15
 El-Badry K., Rix H.-W., Heintz T. M., 2021, *MNRAS*, **506**, 2269
 El-Badry K., Conroy C., Fuller J., Kiman R., van Roestel J., Rodriguez A. C., Burdge K. B., 2022, *MNRAS*, **517**, 4916
 Fabrycky D., Tremaine S., 2007, *ApJ*, **669**, 1298
 Forbes J. C., Loeb A., 2019, *ApJ*, **871**, 227
 Foreman-Mackey D., Hogg D. W., Lang D., Goodman J., 2013, *PASP*, **125**, 306
 Gaia Collaboration et al., 2021a, *A&A*, **649**, A1
 Gaia Collaboration et al., 2021b, *A&A*, **649**, A6
 Gaia Collaboration et al., 2022, *arXiv e-prints*, p. arXiv:2208.00211
 Garraffo C., Drake J. J., Cohen O., 2015, *ApJ*, **807**, L6
 Geier S., et al., 2011, *ApJ*, **731**, L22
 Gelino C. R., Kirkpatrick J. D., Burgasser A. J., 2009, in Stempels E., ed., *American Institute of Physics Conference Series Vol. 1094*, 15th Cambridge Workshop on Cool Stars, Stellar Systems, and the Sun. pp 924–927, doi:10.1063/1.3099269
 Grether D., Lineweaver C. H., 2006, *ApJ*, **640**, 1051
 Grieves N., et al., 2021, *A&A*, **652**, A127
 Gullikson K., Dodson-Robinson S., Kraus A., 2014, *AJ*, **148**, 53
 Harding L. K., et al., 2016, *MNRAS*, **457**, 3036
 Hodžić V., et al., 2018, *MNRAS*, **481**, 5091
 Holman M., Touma J., Tremaine S., 1997, *Nature*, **386**, 254
 Hsu C.-C., Burgasser A. J., Theissen C. A., 2023, *ApJ*, **945**, L6
 Hwang H.-C., Zakamska N. L., 2020, *MNRAS*, **493**, 2271
 Irwin J., et al., 2009, *ApJ*, **701**, 1436
 Ivezić Ž., et al., 2019, *ApJ*, **873**, 111
 Jackman J. A. G., et al., 2019, *MNRAS*, **489**, 5146
 Jackson R. J., Jeffries R. D., Deliyannis C. P., Sun Q., Douglas S. T., 2019, *MNRAS*, **483**, 1125
 Jaehnig K., Somers G., Stassun K. G., 2019, *ApJ*, **879**, 39
 Kaiser N., et al., 2002, in Tyson J. A., Wolff S., eds, *Society of Photo-Optical Instrumentation Engineers (SPIE) Conference Series Vol. 4836*, Survey and Other Telescope Technologies and Discoveries. pp 154–164, doi:10.1117/12.457365
 Kawaler S. D., 1988, *ApJ*, **333**, 236
 Kesseli A. Y., West A. A., Veyette M., Harrison B., Feldman D., Bochanski J. J., 2017, *ApJS*, **230**, 16
 Kesseli A. Y., Muirhead P. S., Mann A. W., Mace G., 2018, *AJ*, **155**, 225
 Kirkpatrick J. D., et al., 2021, *ApJS*, **253**, 7
 Kovács G., Zucker S., Mazeh T., 2002, *A&A*, **391**, 369
 Lanza A. F., Rodono M., Rosner R., 1998, *MNRAS*, **296**, 893
 Littlefair S. P., et al., 2014, *MNRAS*, **445**, 2106
 López-Morales M., Ribas I., 2005, *ApJ*, **631**, 1120
 Lourie N. P., et al., 2020, in Evans C. J., Bryant J. J., Motohara K., eds, *Society of Photo-Optical Instrumentation Engineers (SPIE) Conference Series Vol. 11447*, Ground-based and Airborne Instrumentation for Astronomy VIII. p. 114479K ([arXiv:2102.01109](https://arxiv.org/abs/2102.01109)), doi:10.1117/12.2561210
 Lubow S. H., Shu F. H., 1975, *ApJ*, **198**, 383
 Ma B., Ge J., 2014, *MNRAS*, **439**, 2781
 Mace G. N., 2014, PhD thesis, University of California, Los Angeles
 Mainzer A., et al., 2014, *ApJ*, **792**, 30
 Mann A. W., Brewer J. M., Gaidos E., Lépine S., Hilton E. J., 2013, *AJ*, **145**, 52
 Mann A. W., et al., 2019, *ApJ*, **871**, 63
 Marcy G. W., Butler R. P., 2000, *PASP*, **112**, 137
 Marley M. S., et al., 2021, *ApJ*, **920**, 85
 Matt S. P., Brun A. S., Baraffe I., Bouvier J., Chabrier G., 2015, *ApJ*, **799**, L23
 Maxted P. F. L., 2016, *A&A*, **591**, A111
 McLaughlin D. B., 1924, *ApJ*, **60**, 22
 McMillan P. J., 2017, *MNRAS*, **465**, 76
 Mullan D. J., MacDonald J., 2001, *ApJ*, **559**, 353
 Nefs S. V., et al., 2012, *MNRAS*, **425**, 950
 Newton E. R., Irwin J., Charbonneau D., Berlind P., Calkins M. L., Mink J., 2017, *ApJ*, **834**, 85
 Palle E., et al., 2021, *A&A*, **650**, A55
 Parsons S. G., et al., 2017, *MNRAS*, **471**, 976
 Parsons S. G., et al., 2018, *MNRAS*, **481**, 1083
 Parviainen H., et al., 2020, *A&A*, **633**, A28
 Peters P. C., 1964, *Physical Review*, **136**, 1224
 Phillips M. W., et al., 2020, *A&A*, **637**, A38
 Pollacco D. L., et al., 2006, *PASP*, **118**, 1407
 Prša A., Zwitter T., 2005, *ApJ*, **628**, 426
 Raghavan D., et al., 2010, *ApJS*, **190**, 1
 Rappaport S., Verbunt F., Joss P. C., 1983, *ApJ*, **275**, 713
 Rappaport S., Vanderburg A., Schwab J., Nelson L., 2021, *ApJ*, **913**, 118
 Reiners A., Basri G., 2008, *ApJ*, **684**, 1390
 Ricker G. R., et al., 2015, *Journal of Astronomical Telescopes, Instruments, and Systems*, **1**, 014003
 Rossiter R. A., 1924, *ApJ*, **60**, 15
 Rothman L. S., et al., 2009, *J. Quant. Spec. Radiat. Transf.*, **110**, 533

- Sainsbury-Martinez F., Casewell S. L., Lothringer J. D., Phillips M. W., Tremblin P., 2021, *A&A*, **656**, A128
- Salpeter E. E., 1992, *ApJ*, **393**, 258
- Schatzman E., 1962, *Annales d’Astrophysique*, **25**, 18
- Schreiber M. R., et al., 2010, *A&A*, **513**, L7
- Seabroke G. M., Gilmore G., 2007, *MNRAS*, **380**, 1348
- Sebastian D., et al., 2022, *MNRAS*, **516**, 636
- Sharma S., et al., 2014, *ApJ*, **793**, 51
- Sheinis A. I., Bolte M., Epps H. W., Kibrick R. I., Miller J. S., Radovan M. V., Bigelow B. C., Sutin B. M., 2002, *PASP*, **114**, 851
- Sills A., Pinsonneault M. H., Terndrup D. M., 2000, *ApJ*, **534**, 335
- Skrutskie M. F., et al., 2006, *AJ*, **131**, 1163
- Soszyński I., et al., 2015, *Acta Astron.*, **65**, 39
- Spergel D., et al., 2015, *arXiv e-prints*, p. arXiv:1503.03757
- Stamatellos D., Whitworth A. P., 2009, *MNRAS*, **392**, 413
- Steele P. R., et al., 2013, *MNRAS*, **429**, 3492
- Stepien K., 2006, *Acta Astron.*, **56**, 347
- Tokovinin A., Thomas S., Sterzik M., Udry S., 2006, *A&A*, **450**, 681
- Triaud A. H. M. J., et al., 2017, *A&A*, **608**, A129
- Watson C. A., Marsh T. R., 2010, *MNRAS*, **405**, 2037
- Wright E. L., et al., 2010, *AJ*, **140**, 1868
- Yu J., Liu C., 2018, *MNRAS*, **475**, 1093
- Zhang Z. H., Homeier D., Pinfield D. J., Lodieu N., Jones H. R. A., Allard F., Pavlenko Y. V., 2017, *MNRAS*, **468**, 261

This paper was built using the Open Journal of Astrophysics L^AT_EX template. The OJA is a journal which

provides fast and easy peer review for new papers in the **astro-ph** section of the arXiv, making the reviewing process simpler for authors and referees alike. Learn more at <http://astro.theoj.org>.